

Ultra-fast dynamics and solvent-dependent deactivation kinetics of BODIPY molecular rotors

Tomislav Suhina,^{†,‡} Saeed Amirjalayer,[¶] Sander Woutersen,[†] Daniel Bonn,[‡] and
Albert M. Brouwer^{*,†}

[†]*Van't Hoff Institute for Molecular Sciences, University of Amsterdam, PO Box 94157,
1090 GD Amsterdam, The Netherlands*

[‡]*Van der Waals-Zeeman Institute of Physics, University of Amsterdam, PO Box 94485,
1090 GL Amsterdam, The Netherlands*

[¶]*Center for Nanotechnology (CeNTech) and Physical Institute, University of Münster,
Heisenbergstrasse 11, 48149 Münster, Germany*

E-mail: a.m.brouwer@uva.nl

Contents

Determining the position of spectral maxima

As noted in the main text, Stokes shifts exhibited by **1** are very small. This makes the task of finding peak locations precisely very important. Positions of absorption and emission maxima in pure solvents and solvent mixtures were determined in the same way, which is described below.

The spectral data was obtained by measuring fluorescence counts in 1 nm steps. Due to the low fluorescence quantum yield, the data were too noisy to determine the position of spectral maximum with sufficient certainty. First, the spectra were converted to the

wavenumber representation. Because such spectra are not uniformly sampled, cubic spline interpolation was used in order to obtain uniformly sampled data (which produces better fits). Since we were interested in the position of the spectral maxima, we have selected the data points which have at least 85 % of the maximal count value and used a Gaussian function to fit the peaks. A typical result of this procedure is shown in Fig. S1. Errors were estimated from uncertainties (95 % confidence interval) of the Gaussian fit (error bars in Fig. S3).

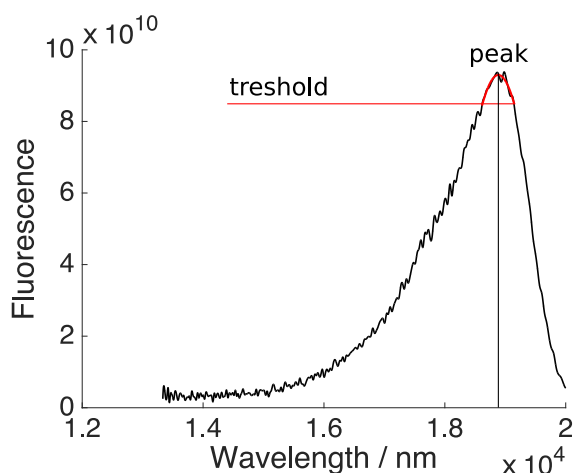


Figure S1: Representative example demonstrating the fitting procedure used in determining location of the excitation / emission maxima.

Stokes shifts

Although absorption and emission spectra of **1** exhibit hypsochromic shifts, the Stokes shifts increase as a function of solvent's orientation polarization and could be quantified, as described below.

The difference between the dipole moment of the ground state and that of the excited state ($\Delta\mu$) can be experimentally estimated from the Lippert-Mataga (LM) expression, where Stokes shifts are expressed as a function of the solvent's orientation polarization.¹ In its commonly used form, LM only considers the polarization induced in a solvent by the ground- and excited-state dipoles.² Polarizability of the solute is taken into account in the polarizable

point-dipole dielectric continuum model,³⁻⁵ in which the Stokes shift is expressed as a function of $d_c(\epsilon_r) - d_c(n^2)$ defined in Eqs. 1 and 2, where ϵ_r represents relative permittivity and n refractive index of the solvent. In these expressions, c is a solute polarizability parameter which can be expressed as $c = \alpha/a^3$, where α is a solute isotropic polarizability (256 Bohr³) and a (9.77 Bohr) is the effective radius of the solute. Both parameters were obtained from DFT calculations. In the case of **1**, c is estimated to be 0.27. In order to obtain the dipole moment difference we have measured absorption and emission spectra of **1** in a series of pure solvents and in toluene/MeCN mixtures for which the values of refractive indices⁶ and dielectric constants⁷ can be interpolated based on the values reported in the literature.

$$\nu_{abs} - \nu_{em} = \frac{2}{hc} [d_c(\epsilon_r) - d_c(n^2)] \frac{\Delta\mu_{S_1-S_0}^2}{a^3} + h\nu_{abs}^0 - h\nu_{em}^0 \quad (1)$$

$$d_c(x) = \frac{d_0(x)}{1 - 2cd_0(x)} = \frac{x - 1}{2(1 - c)x + (1 + 2c)} \quad (2)$$

$$d_0(x) = \frac{x - 1}{2x + 1} \quad (3)$$

$$\Delta\mu = \sqrt{9.9316 \times 10^{-5} \times slope \times a^3} \quad (4)$$

Figure S2 shows spectral maxima positions plotted against modified solvent's orientational polarization function ($d_c(\epsilon) - d_c(n^2)$) in mixtures of toluene and MeCN (0-100 % v/v). At relatively low MeCN concentrations, the relationship between the spectral maxima and $d_c(\epsilon) - d_c(n^2)$ is linear and therefore indicates that specific interactions do not play a significant role. As MeCN concentrations increase (>70 % by volume), deviations from the linear trend are observed. A larger point scatter can be observed in case of the emission maxima. This occurs due to the difficulties which are inherent to emission spectra measurements for fluorophores with very low fluorescence quantum yields.

Fig. S3 shows the Stokes shift as a function of $d_c(\epsilon_r) - d_c(n^2)$ for pure solvents (a) and toluene/MeCN mixtures (b) in which specific interactions can be neglected (see Fig.

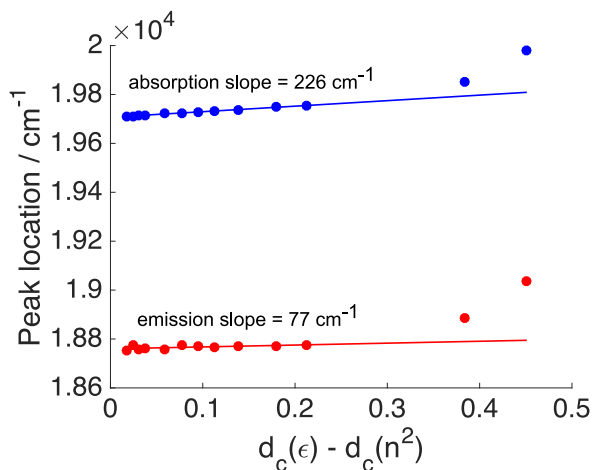


Figure S2: Measured spectral maxima plotted against the solvent polarity function in toluene/MeCN mixtures.

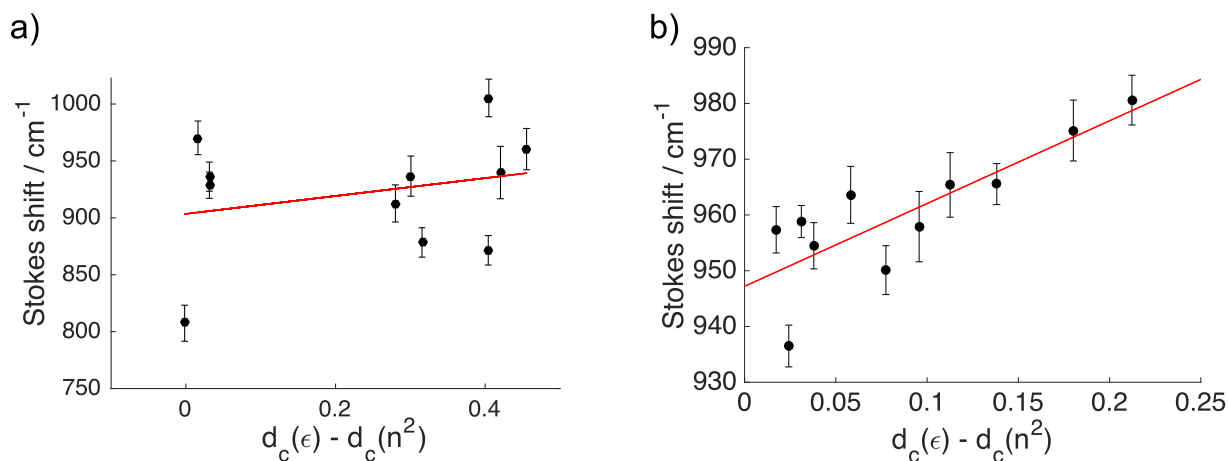


Figure S3: Stokes shifts of **1** as a function of solvent polarity. a) Pure solvents; b) toluene/MeCN mixtures.

S2). The linear fit of the Stokes shift *vs* the modified orientational polarization function $d_c(\epsilon_r) - d_c(n^2)$ in pure solvents produces a slope of $85 \pm 210 \text{ cm}^{-1}$. The points obtained for pure solvents are very scattered, and a linear correlation between the Stokes' shifts and orientational polarization function can not be ascertained (error bar of 210 cm^{-1} with 95% confidence level). Nonetheless, from Eq. 4, the slope of 85 cm^{-1} , and the effective solute radius of $a = 5.17 \text{ \AA}$ we estimate the difference between ground- and excited-state dipole moments to be $\Delta\mu = 1.1 \text{ D}$. The points are significantly less scattered in toluene/MeCN mixtures, where specific interactions are small, and refractive indices/dielectric constants change systematically. An obvious correlation between the Stokes shift and the $d_c(\epsilon_r) - d_c(n^2)$ parameter can be observed for these data, where we obtain a slope of $148 \pm 79 \text{ cm}^{-1}$. This corresponds to a dipole moment difference of $\Delta\mu = 1.4 \pm 0.9 \text{ D}$.

Dependence of Fluorescence Quantum Yields on Solvent Polarity and Viscosity

In order to check whether the solvent polarity plays a significant role in fluorescence deactivation of **1**, we measured its fluorescence quantum yields in a range of aprotic solvents. The quantum yields were determined relative to the fluorescence quantum yield of **1** in MeCN, which was measured relative to fluorescein in 0.1 M NaOH ($\Phi_f = 0.89$).⁸

Time correlated single photon counting

Experimental details

Fluorescence decay curves of **1** were measured using time-correlated single photon counting (TCSPC). For excitation, we used a tunable Ti:sapphire laser (Chameleon Ultra, Coherent), operating at a repetition rate of 80 MHz, with pulse width of 150 fs. An APE pulse picker was used to reduce the rate to 8 MHz. The excitation wavelength of 488 nm was obtained by

Table S1: Fluorescence data of **1** measured in different solvents.

Solvent	η^a /cP	ϵ_r^b	$f(\epsilon)^c$	$\Phi_f^d/\%$	$k_{nr}^e \times 10^{-10} \text{ s}^{-1}$	$\lambda_{max,abs}^f/\text{cm}^{-1}$	$\lambda_{max,em}^g/\text{cm}^{-1}$
dioxane	1.37	2.25	0.23	1.43	0.96	19941	19000
EtOAc	0.43	6.02	0.38	0.65	2.12	19931	19014
THF	0.48	7.58	0.41	0.70	1.99	19852	18909
Acetone	0.32	20.7	0.46	0.49	2.86	19940	19000
MeCN	0.35	37.5	0.48	0.50	2.78	19977	19020
DMSO	1.99	46.7	0.48	1.11	1.25	19740	18734
DCM	0.43	8.93	0.42	0.93	1.49	19803	18927
hexane	0.30	1.88	0.18	0.72	1.93	19863	19056
toluene	0.59	2.37	0.24	0.80	1.73	19708	18741
glycerol	1412	42.5	0.48	39.7	0.02	19735	18907

^a Viscosity (η) obtained from ref. 9; ^b Values for relative permittivity (ϵ_r) obtained from ref. 9; ^c Solvent's polarity function $f(\epsilon) = (\epsilon - 1)/(2\epsilon + 1)$; ^d Fluorescence quantum yields; fluorescein in 0.1 M NaOH ($\Phi_f=0.89^8$) was used as a reference; ^e Nonradiative rate calculated from Φ_f ; ^f Absorption maximum; ^g Emission maximum.

frequency doubling (APE SHG unit). The instrument response function (fwhm ~ 24 ps) was determined using scattered light at the excitation wavelength from a ceramic plate placed at 45° . An ORIEL Cornerstone 260 mm monochromator was used with an MCP detector (Hamamatsu R3809U-51). A 488 nm notch filter (placed before the monochromator) was used to block the excitation light. TCSPC histograms were recorded up to $\sim 10^4$ counts in the peak channel, and were fitted using nonlinear least squares with IRF deconvolution using DecFit software^{10,11} written in Python by Nikolai Tkachenko (Tampere University of Technology, Finland), or with home-built macros in IgorPro.

1 in PMMA

To examine fluorescence lifetime of the confined probe, we measured its fluorescence decays in strongly confining polymethyl methacrylate (PMMA) matrix. The curve was fitted by iterative convolution of three exponential functions with the measured instrument response functions. This produced fluorescence lifetimes of $\tau_1 = 11330$ ps (0.2 %), $\tau_2 = 7149$ ps (93.7 %), and $\tau_3 = 915$ ps (6.1 %) with $\chi^2 = 1.08$. The average fluorescence lifetime (7.12 ns) was calculated according to Eq. 5. The fluorescence decay curve of **1** in PMMA matrix is shown

in Fig. S4.

$$\tau_{avg} = \frac{A_1\tau_1^2 + A_2\tau_2^2 + A_3\tau_3^2}{A_1\tau_1 + A_2\tau_2 + A_3\tau_3} \quad (5)$$

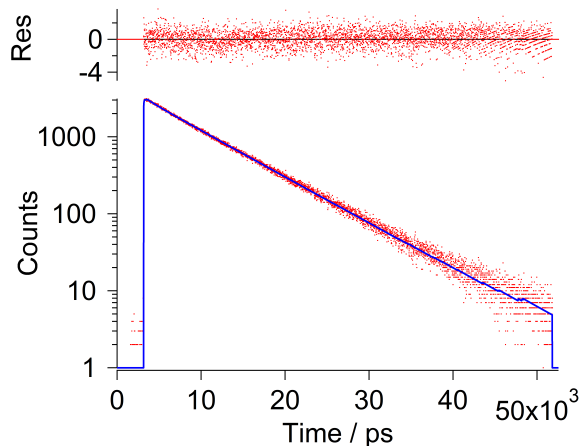


Figure S4: Fluorescence decay of **1** in PMMA.

Additional details on vis-pump/vis-probe measurements of **1**

A rise component can be observed in the vis/vis TA experiments in the ESA region. Representative curves (after filtering of the two most prominent components based on singular value decomposition in order to reduce noise) are shown in Fig. S5.

Stimulated emission time traces monitored at different energies indicate that solvent relaxation takes place on very short time scales. As the emission energy decreases, the rise component becomes longer and pronounced. Time traces taken at 530, 550 and 580 nm for **1** in MeCN are shown in Fig. S6 and look similar to the ones obtained in toluene (not shown). Single-trace fits produce time constants of 0.16, 0.42 and 0.57 ps for time traces monitored at 530, 550 and 580 nm in MeCN, respectively (time constants of the two emissive components have been fixed to 9.4 and 50 ps obtained by global analysis).

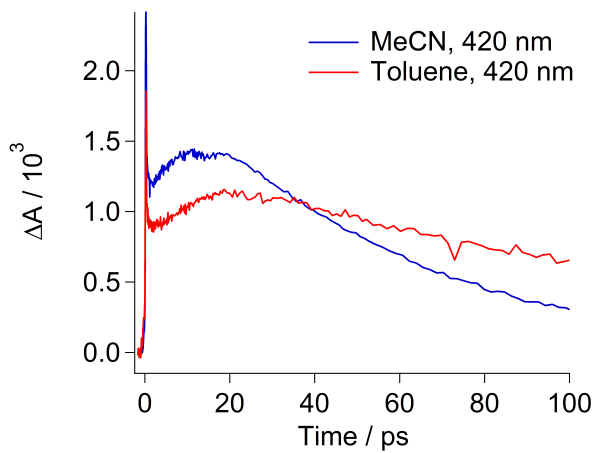


Figure S5: Excited-state absorption time traces obtained by vis-pump/vis-probe measurements for **1** in MeCN.

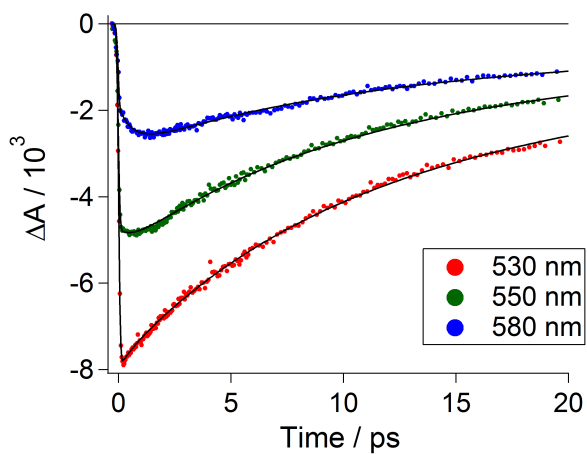


Figure S6: Stimulated emission time traces for **1** in MeCN obtained by vis-pump/vis-probe transient spectroscopy. Fits obtained by global analysis of the whole transient matrix with the sequential model are shown in black.

Calculated vibrational spectra and mode assignment

We calculated ground- and excited-state species vibrational spectra with CAM-B3LYP/6-31G(d) and CAM-B3LYP/6-31+G(d,p) levels of theory in vacuum and with PCM¹² MeCN solvation. We observed modest improvement when the larger basis set was used. Vibrational spectra calculated for vacuum were more similar to the experimental spectra than those calculated with PCM solvation. The experimental and calculated spectra are compared in Fig. 7 in the main text. Fig. S7 shows vibrational modes with their respective frequencies obtained with CAM-B3LYP/6-31+G(d,p) in vacuum. The region $\sim 1520\text{ cm}^{-1}$, where we observe a rise in ESA signal contains only modes associated with the BODIPY core, or the BODIPY core modes mixed with vibrational modes on the phenyl ring.

Excitation energies and potential energy surface scans

Excitation energies and oscillator strengths calculated with the two basis sets for **1** in vacuum are shown in Figure S8. The calculated excitation energies (CAM-B3LYP/6-31+G(d,p)) of **1** decrease from vacuum to MeCN (3.09 eV in vacuum; 2.89 eV in toluene; 2.68 eV in MeCN). Emission energies obtained by calculations follow the same trend (2.88 eV in vacuum; 2.76 eV in toluene; 2.58 eV in MeCN). We attribute the disagreement between the experimental (where we observe blue shift in more polar solvents) and calculated trends to limitations of the PCM model in treating non-electrostatic effects.¹³

The photophysical picture obtained by using partially relaxed potential energy surface scans with the larger 6-31+G(d,p) basis set is consistent with the one obtained from CAM-B3LYP/6-31G(d) (Fig. S10). Twisting is, as in the case of 6-31G(d) basis set accompanied by an abrupt drop in oscillator strength (from 0.34 at B-Phe = 30° to 0.0081 at B-Phe = 20°). Estimated energy barriers are 1.2 kcal mol⁻¹ (at B-Phe = 30°) and 2.3 kcal mol⁻¹ (at B-Phe = 90°). Comparison of the oscillator strengths *vs* P-Phe dihedral are shown in Fig. S11.

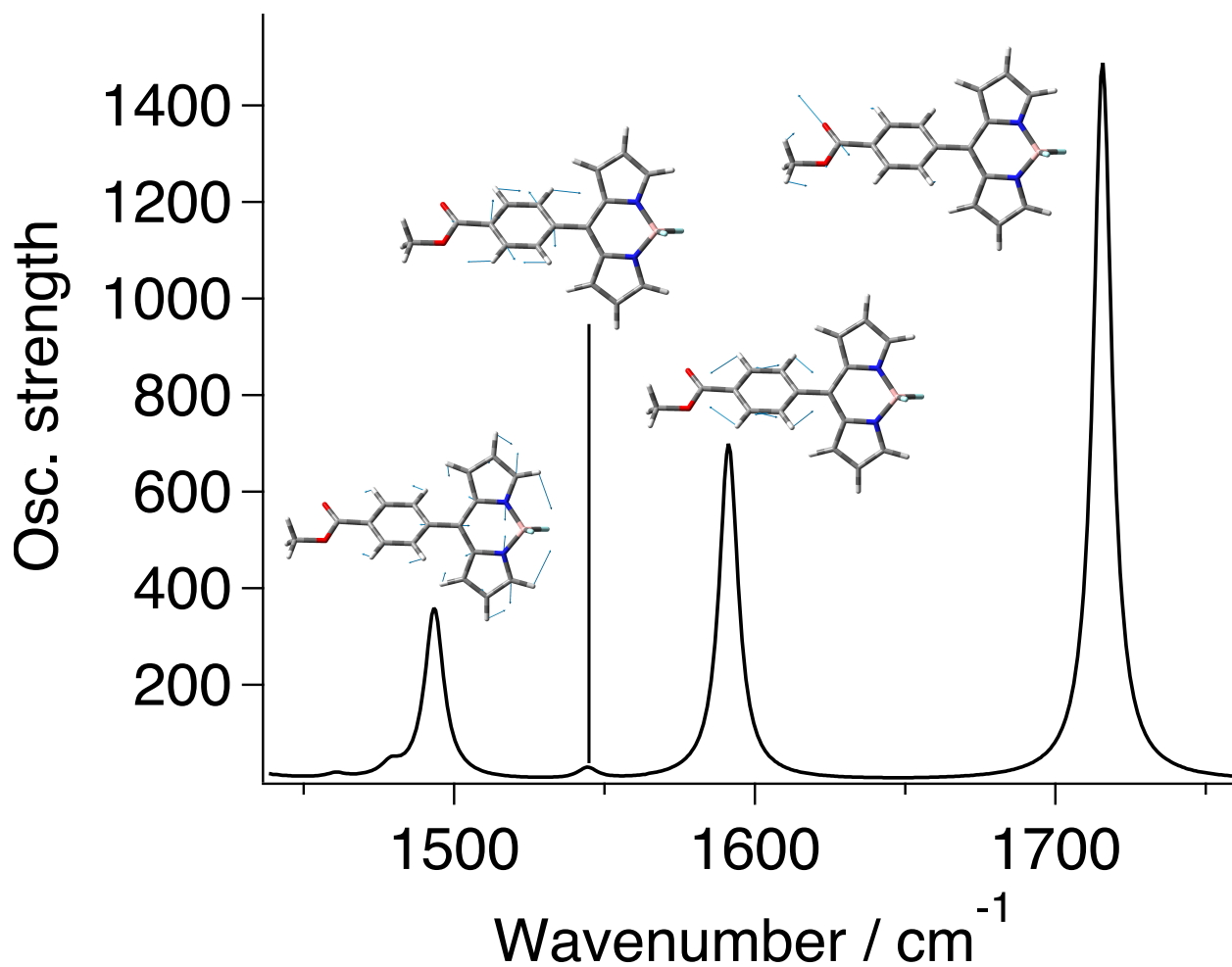


Figure S7: Assignment of the relevant vibrational modes calculated with TD-DFT CAM-B3LYP/6-31+G(d,p) level of theory in vacuum. The band located around 1490 cm^{-1} consist of multiple modes involving the same atoms, and only the most intense one is shown.

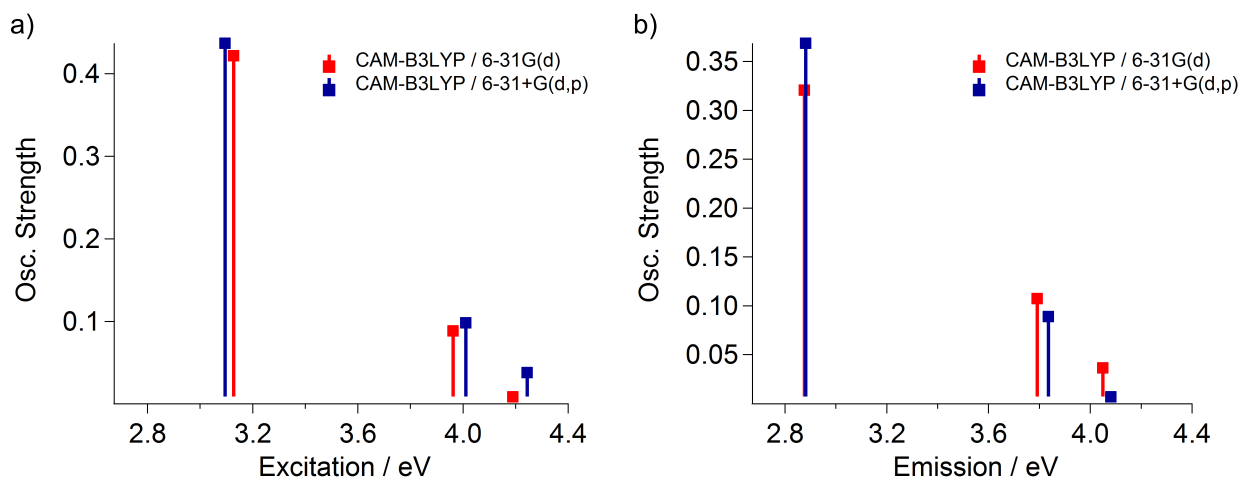


Figure S8: Comparison of the calculated excitation a) and emission b) energies *vs* oscillator strengths obtained with 6-31G(d) and 6-31+G(d,p) in vacuum.

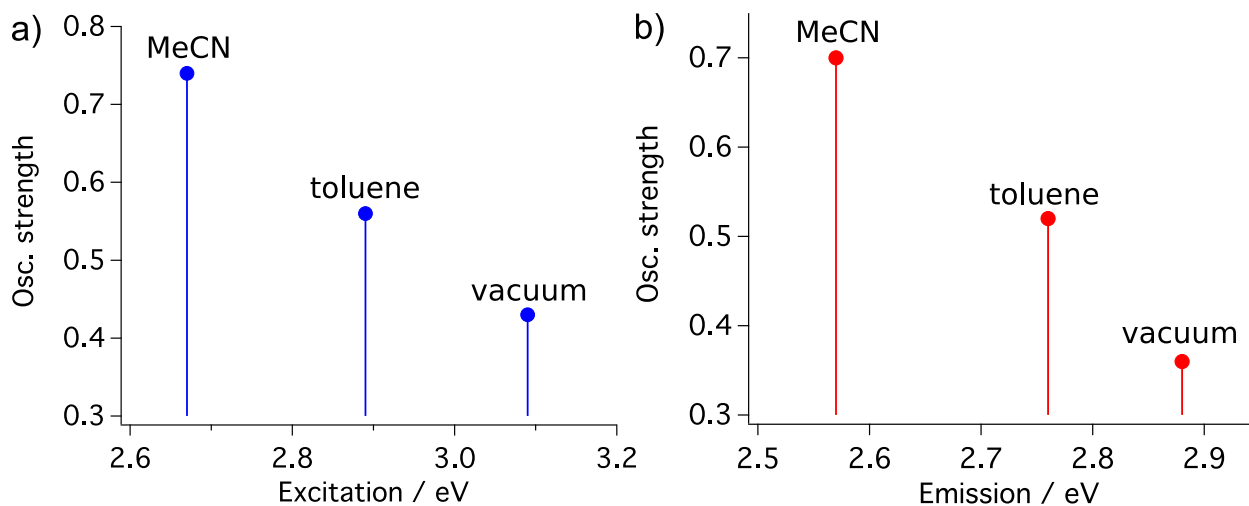


Figure S9: Comparison of the calculated excitation a) and emission b) energies *vs* oscillator strengths obtained with 6-31+G(d,p) in vacuum, toluene and MeCN.

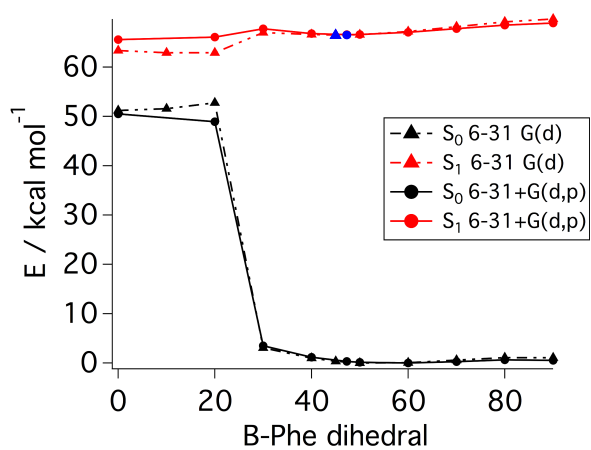


Figure S10: Comparison of the partial potential energy surface scans obtained with TD CAM-B3LYP/6-31G(d) and TD CAM-B3LYP/6-31+G(d,p) levels of theory. Blue markers represent S_1 optimized geometries.

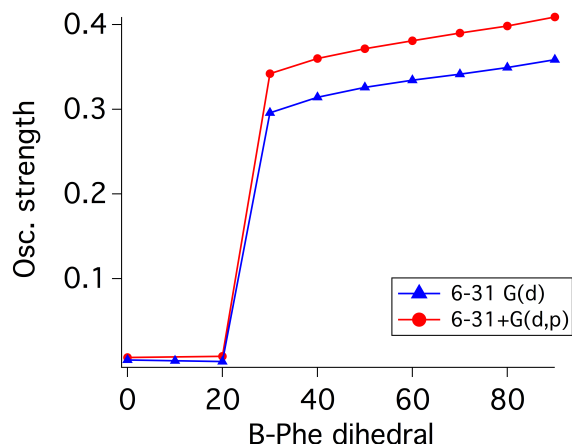


Figure S11: Oscillator strengths obtained with CAM-B3LYP/6-31G(d) and CAM-B3LYP/6-31+G(d,p) level of theory *vs* B-Phe dihedral values.

Discussion

By comparing the 6-31G(d) and 6-31+G(d,p) results, we found that the 6-31+G(d,p) basis set provides modest improvement in the excitation energies and calculated frequencies, but does not change the general trends. The optimized ground state structure (CAM-B3LYP/6-31+G(d,p)) is characterized by the planar BODIPY core (Fig. 7 a), main text) which forms a B-Phe dihedral angle of 57.7° . Including MeCN (or toluene) solvation does not influence the structure significantly in the ground state. Optimization of the first excited state in vacuum results in a slight distortion on the BODIPY core which assumes a butterfly-like shape (see Fig. 8 b) in the main text). The B-Phe dihedral angle, notably, decreases from 57.7° in the ground state to 47.3° in the excited state. Including toluene (or MeCN) solvation results in a planar core geometry of the first excited state. The B-Phe dihedral of the optimized geometries in toluene changes from 57.6° in the ground state to 48.1° in the first excited state. Including MeCN solvation produces dihedrals of 56.7° and 49.9° for the ground and the first excited state, respectively.

The partial excited-state potential energy surface scan in vacuum (6-31G(d) basis set, Figure 9 b) in the main text) reveals the presence of four minima in the scanned range of 0 - 180° . The two of these minima could not be reproduced with the larger basis set

(6-31+G(d,p)). The two minima located near the FC region correspond to the excited-state optimized geometries which are referred to as the LE state. Representative structures of the LE state are shown in Fig. 8 b) (main text). These structures are characterized by relatively large oscillator strength values ($f=0.32$ at CAM-B3LYP/6-31G(d) optimized geometry). The other two structures (see Fig. S12), which represent global minima (but only with the smaller basis set; see below), are not expected to show fluorescence due to the low oscillator strength values ($f=0.002$ at CAM-B3LYP/6-31G(d) optimized geometry). In addition, large structural changes in the core geometry (Fig. S12) take place suddenly once the dihedral values change from $\sim 30\text{-}20^\circ$ with CAM-B3LYP level of theory (in the case of both examined basis sets). This, in combination with oscillator strength drop and general proximity of the ground and excited-state potential energy surfaces strongly suggests that surface crossing occurs near these coordinates.

As in the ground-state calculation, two LE state minima are located on the S_1 surface and correspond to the two excited-state conformers. These minima are separated by a small energy barrier (~ 3.2 kcal mol $^{-1}$) which is somewhat greater than the barrier which separates the two conformers in the ground state. The decrease in B-Phe dihedral (or its increase towards 180°) results in S_1 energy drop, which is accompanied by a rise in energy of the ground-state structure. The estimated energy barrier for this rotation is only 0.5 kcal mol $^{-1}$, indicating that this motion occurs easily at room temperature.

Although the change in B-Phe angle towards 0° (or 180°) leads to a global minimum in the case of the 6-31G(d) basis set, geometry optimizations become increasingly difficult as dihedral angle approaches the extreme values. Change in dihedral is also accompanied by a sudden drop in oscillator strength ($f = 0.3 \rightarrow 0.002$, from 30° to 20° , see Fig. S11). Since we do not experimentally observe dark transient intermediates associated with these highly distorted minima, the presence of a conical intersection near these coordinates is the most likely explanation for the observed fluorescence deactivation and its high efficiency.

We were not able to find the minimum that would be associated with the FC state (due

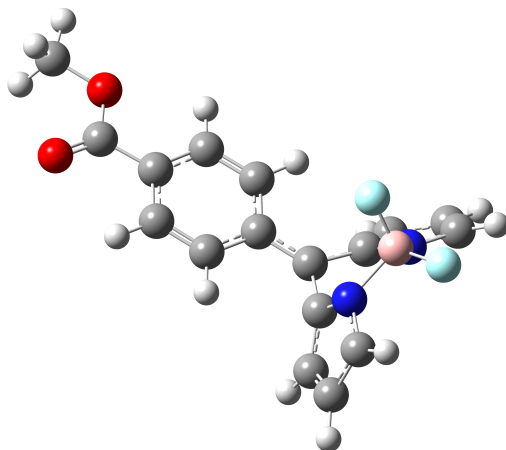


Figure S12: The structure of the apparent global minimum (B-Phe = 2 deg) reached by B-Phe dihedral twist optimized with CAM-B3LYP/6-31G(d) level of theory. The optimization with 6-31+G(d,p) does not lead to a minimum.

to which ~ 10 ps time constant is observed). The most likely reason is the overall flatness of the excited-state potential energy surface, since even increasing the grid size and varying the starting geometries did not result in stable geometries different from the one attributed to the LE state (or the distorted structure with B-Phe dihedral ~ 0). It is likely that more advanced theoretical models would need to be used to find such geometry (if it exists), but such calculations are out of the scope of the current paper.

Relevant Geometries

Table S2: XYZ coordinates of CAM-B3LYP/6-31+G(d,p) optimized ground-state geometry of **1** in vacuum.

C	1.58643	-1.20697	-0.09432
N	2.9758	-1.19706	-0.12717
B	3.88431	0.06577	-0.07805
N	2.91479	1.27417	0.06933
C	1.52779	1.20853	0.12181
C	0.86022	-0.01811	0.0336
C	1.15921	-2.5482	-0.24536
C	2.29711	-3.32906	-0.35528
C	3.3952	-2.45379	-0.28108
C	3.27479	2.55037	0.21407
C	2.13795	3.36336	0.36792
C	1.03903	2.52259	0.31673
F	4.60951	0.17321	-1.25791
F	4.73656	0.00405	1.01641
C	-0.62094	-0.05713	0.0761
C	-1.37253	0.65654	-0.86293
C	-2.75984	0.61535	-0.83142
C	-3.41334	-0.12964	0.15036
C	-2.66919	-0.83713	1.09394
C	-1.2829	-0.80738	1.05395
C	-4.89943	-0.20258	0.23443
O	-5.50204	-0.84122	1.06917
O	-5.5093	0.51818	-0.71815
C	-6.94181	0.4915	-0.69668
H	0.13175	-2.87944	-0.27786
H	2.3496	-4.4003	-0.48204
H	4.45183	-2.67672	-0.33906
H	4.31944	2.82998	0.20922
H	2.14056	4.43423	0.50801
H	-0.00075	2.79583	0.41969
H	-0.86492	1.22756	-1.63267
H	-3.33967	1.15893	-1.56746
H	-3.19358	-1.40542	1.85395
H	-0.70649	-1.34964	1.7955
H	-7.31326	0.8876	0.25
H	-7.2576	1.11873	-1.52818
H	-7.30298	-0.53049	-0.8236

Table S3: XYZ coordinates of CAM-B3LYP/6-31+G(d,p) optimized ground-state geometry of **1** in MeCN.

C	1.58575	-1.20506	-0.10364
N	2.97743	-1.1924	-0.13424
B	3.86815	0.06638	-0.06108
N	2.91441	1.27378	0.06399
C	1.52492	1.2086	0.11735
C	0.85564	-0.01785	0.02807
C	1.16217	-2.54384	-0.26534
C	2.30238	-3.32458	-0.38004
C	3.39858	-2.4527	-0.29754
C	3.27358	2.55593	0.20377
C	2.13734	3.36529	0.35364
C	1.03769	2.52179	0.30672
F	4.65096	0.17598	-1.21951
F	4.71866	0.00206	1.05222
C	-0.62443	-0.05932	0.07257
C	-1.3788	0.67131	-0.85149
C	-2.76567	0.6268	-0.81622
C	-3.41549	-0.13778	0.15381
C	-2.66685	-0.8617	1.08185
C	-1.28079	-0.82966	1.03875
C	-4.90159	-0.20956	0.23499
O	-5.50559	-0.86707	1.06169
O	-5.50885	0.52601	-0.69764
C	-6.94562	0.51405	-0.69047
H	0.13574	-2.87789	-0.30066
H	2.35559	-4.39483	-0.51475
H	4.45384	-2.68239	-0.35511
H	4.31597	2.84421	0.19828
H	2.13864	4.43705	0.4868
H	-0.00182	2.79769	0.40496
H	-0.87862	1.25843	-1.61338
H	-3.34383	1.18542	-1.5418
H	-3.17943	-1.44791	1.83561
H	-0.70484	-1.38582	1.76976
H	-7.3198	0.89621	0.26017
H	-7.24519	1.16414	-1.50933
H	-7.31395	-0.50004	-0.85082

Table S4: XYZ coordinates of TD CAM-B3LYP/6-31+G(d,p) optimized excited-state geometry of **1** in vacuum.

C	1.6212	1.2265	0.0177
N	3.0286	1.1535	0.0739
B	3.87	-0.1282	0.2754
N	2.9139	-1.2778	-0.1095
C	1.5129	-1.1903	-0.2147
C	0.8294	0.0503	-0.0799
C	1.2639	2.5968	0.0702
C	2.4426	3.3252	0.1362
C	3.5098	2.3952	0.1398
C	3.276	-2.535	-0.3652
C	2.129	-3.317	-0.6459
C	1.0289	-2.4768	-0.5567
F	4.2629	-0.2426	1.6067
F	4.982	-0.1197	-0.5568
C	-0.6341	0.0981	-0.096
C	-1.3819	-0.7986	0.687
C	-2.7668	-0.7599	0.6905
C	-3.4456	0.1695	-0.1015
C	-2.7157	1.0574	-0.8935
C	-1.3311	1.0269	-0.8885
C	-4.9281	0.2527	-0.139
O	-5.5513	1.0501	-0.8074
O	-5.5215	-0.6563	0.6528
C	-6.9528	-0.6274	0.6661
H	0.2577	2.9851	0.0697
H	2.5457	4.3995	0.1916
H	4.5745	2.571	0.211
H	4.3179	-2.8242	-0.3475
H	2.132	-4.3688	-0.8939
H	-0.0041	-2.7259	-0.745
H	-0.8647	-1.508	1.324
H	-3.3295	-1.4439	1.3144
H	-3.254	1.7624	-1.5174
H	-0.7801	1.7004	-1.5351
H	-7.3454	-0.8112	-0.3357
H	-7.2546	-1.4188	1.3497
H	-7.3095	0.3428	1.0166

Table S5: XYZ coordinates of TD CAM-B3LYP/6-31+G(d,p) optimized excited-state geometry of **1** in MeCN.

C	1.59701	-1.2067	-0.10695
N	2.99864	-1.17574	-0.12836
B	3.8856	0.07643	-0.05561
N	2.92554	1.26915	0.06886
C	1.52569	1.2104	0.12307
C	0.83128	-0.02153	0.02736
C	1.1947	-2.56462	-0.27672
C	2.34597	-3.32172	-0.38532
C	3.44194	-2.43108	-0.29247
C	3.29597	2.55034	0.21231
C	2.15203	3.36926	0.36633
C	1.04723	2.53999	0.318
F	4.67465	0.19022	-1.21191
F	4.74305	0.01548	1.05502
C	-0.63919	-0.06881	0.06555
C	-1.40549	0.7672	-0.76036
C	-2.79132	0.72196	-0.72887
C	-3.44525	-0.15857	0.13601
C	-2.6921	-0.99279	0.96419
C	-1.30728	-0.95133	0.92804
C	-4.9274	-0.24069	0.20763
O	-5.53432	-0.99863	0.94278
O	-5.53825	0.60852	-0.62339
C	-6.97422	0.59054	-0.61674
H	0.17446	-2.91298	-0.32302
H	2.4206	-4.39079	-0.52463
H	4.50046	-2.6475	-0.34805
H	4.34004	2.83398	0.21123
H	2.16567	4.441	0.50443
H	0.0108	2.82222	0.42074
H	-0.91064	1.43977	-1.45222
H	-3.3682	1.36565	-1.38172
H	-3.20274	-1.66813	1.64109
H	-0.73646	-1.59019	1.59276
H	-7.34973	0.84842	0.37445
H	-7.27754	1.3375	-1.34693
H	-7.34006	-0.39646	-0.90304

Table S6: XYZ coordinates of TD CAM-B3LYP/6-31+G(d,p) partially optimized excited-state geometry (B-Phe = 30, barrier on PES near conical intersection) of **1** in vacuum.

C	1.65095	1.24036	-0.05816
N	3.05427	1.12612	0.03092
B	3.84742	-0.16523	0.33169
N	2.8869	-1.29884	-0.07724
C	1.49604	-1.18236	-0.24593
C	0.82587	0.07936	-0.16717
C	1.34358	2.62556	-0.02124
C	2.54342	3.31505	0.05859
C	3.57667	2.3506	0.0923
C	3.24138	-2.55906	-0.32455
C	2.09863	-3.3182	-0.67217
C	1.01221	-2.45875	-0.63128
F	4.14888	-0.2393	1.68891
F	5.00961	-0.21422	-0.42652
C	-0.63023	0.14886	-0.1025
C	-1.37803	-0.88699	0.49427
C	-2.76121	-0.85068	0.52729
C	-3.45479	0.205	-0.06976
C	-2.73335	1.21936	-0.70176
C	-1.35047	1.19168	-0.72215
C	-4.93608	0.28941	-0.07
O	-5.57009	1.1911	-0.57666
O	-5.5177	-0.74771	0.55683
C	-6.94845	-0.72491	0.59632
H	0.35775	3.05905	-0.03085
H	2.67922	4.386	0.10793
H	4.64479	2.48892	0.18987
H	4.27692	-2.86343	-0.25873
H	2.09542	-4.36669	-0.93363
H	-0.00867	-2.68947	-0.89173
H	-0.8621	-1.69471	0.99918
H	-3.3126	-1.64048	1.02342
H	-3.27846	2.01855	-1.19185
H	-0.8221	1.95415	-1.27912
H	-7.35649	-0.73417	-0.41604
H	-7.24017	-1.62321	1.13757
H	-7.29976	0.1694	1.11418

Table S7: XYZ coordinates of TD CAM-B3LYP/6-31+G(d,p) partially optimized excited-state geometry (B-Phe = 20, past conical intersection) of **1** in vacuum.

C	1.79389	1.18694	-0.46582
N	2.64051	1.24707	0.6295
B	3.03603	-0.1804	1.23492
N	2.82985	-1.14448	0.01258
C	1.67476	-1.07969	-0.7867
C	0.85414	0.05709	-0.56769
C	2.17904	2.19501	-1.39117
C	3.16786	2.9368	-0.77839
C	3.48895	2.26167	0.43191
C	3.46471	-2.29008	-0.26247
C	2.76235	-2.99401	-1.25445
C	1.63624	-2.24267	-1.57781
F	2.19331	-0.51532	2.2686
F	4.36732	-0.14739	1.60368
C	-0.56016	0.11387	-0.42431
C	-1.29917	-1.04181	-0.07404
C	-2.66756	-0.98537	0.09119
C	-3.35048	0.23017	-0.05678
C	-2.63158	1.38717	-0.36737
C	-1.26272	1.33464	-0.55073
C	-4.8182	0.34362	0.11466
O	-5.44618	1.37532	-0.00592
O	-5.40094	-0.82891	0.42278
C	-6.81885	-0.78612	0.60788
H	1.69459	2.38869	-2.33674
H	3.636	3.84144	-1.13773
H	4.33169	2.41469	1.09095
H	4.36413	-2.56694	0.26932
H	3.05602	-3.94365	-1.67866
H	0.88297	-2.4679	-2.31945
H	-0.76936	-1.97347	0.09015
H	-3.22045	-1.87637	0.36354
H	-3.17157	2.32174	-0.47098
H	-0.72432	2.23646	-0.81921
H	-7.31162	-0.44887	-0.30594
H	-7.11304	-1.80587	0.85025
H	-7.0757	-0.10641	1.42247

References

- (1) Mataga, N.; Kaifu, Y.; Koizumi, M. *Bull. Chem. Soc. Jpn.* **1956**, *29*, 465–470.
- (2) Lakowicz, J. R. *Principles of Fluorescence Spectroscopy, 3rd Ed*; Springer Science & Business Media, 2006.
- (3) Arzhantsev, S.; Zachariasse, K. A.; Maroncelli, M. *J. Phys. Chem. A* **2006**, *110*, 3454–3470.
- (4) Dahl, K.; Biswas, R.; Ito, N.; Maroncelli, M. *J. Phys. Chem. B* **2005**, *109*, 1563–1585.
- (5) Jin, H.; Liang, M.; Arzhantsev, S.; Li, X.; Maroncelli, M. *J. Phys. Chem. B* **2010**, *114*, 7565–7578.
- (6) Shams, A. K. *J. Al-Nahrain Univ.* **2011**, *14*, 75–85.
- (7) Ritzoulis, G.; Papadopoulos, N.; Jannakoudakis, D. *J. Chem. Eng. Data* **1986**, *31*, 146–148.
- (8) Würth, C.; Grabolle, M.; Pauli, J.; Spieles, M.; Resch-Genger, U. *Nat. Protoc.* **2013**, *8*, 1535–1550.
- (9) Haynes, W. M. *CRC handbook of chemistry and physics*; CRC press, 2014.
- (10) Lehtivuori, H.; Efimov, A.; Lemmetyinen, H.; Tkachenko, N. V. *Chem. Phys. Lett.* **2007**, *437*, 238–242.
- (11) Lehtivuori, H.; Kumpulainen, T.; Efimov, A.; Lemmetyinen, H.; Kira, A.; Imahori, H.; Tkachenko, N. V. *J. Phys. Chem. C* **2008**, *112*, 9896–9902.
- (12) Tomasi, J.; Mennucci, B.; Cammi, R. *Chem. Rev.* **2005**, *105*, 2999–3094.
- (13) Mennucci, B.; Tomasi, J.; Cammi, R.; Cheeseman, J.; Frisch, M.; Devlin, F.; Gabriel, S.; Stephens, P. *J. Phys. Chem. A* **2002**, *106*, 6102–6113.